

Coherent Structures in One-dimensional Buneman Instability Nonlinear Simulations

I H Hutchinson

Plasma Science and Fusion Center, MIT, Cambridge, MA 02139, USA

November 21, 2024

Abstract

Long-duration one-dimensional PIC simulations are presented of Buneman-unstable, initially Maxwellian, electron and ion distributions shifted with respect to one another, providing detailed phase-space videos of the time-dependence. The final state of high initial ion temperature cases is dominated by fast electron holes, but when initial ion temperature is less than approximately four times the electron temperature, ion density modulation produces potential perturbations of approximately ion-acoustic character, modified by the electron distribution shift. Early in the nonlinear phase, they often have electron holes trapped in them (“coupled hole-solitons”: CHS). In high-available-energy cases, when major broadening of the electron distribution occurs, both electron holes and coupled hole-solitons can be reflected, giving persistent counter-propagating potential peaks. Analytical theory is presented of steady nonlinear potential structures in model nonlinear particle distribution plasmas with Buneman unstable parameters. It compares favorably in some respects with the nonlinear simulations, but not with the later phases when the electron velocity distributions are greatly modified.

1 Introduction

The linear stability of initially uniform plasma with relative drift velocity of electrons and ions v_{de} is a long-settled classic problem addressed in many textbooks. When v_{de} is smaller than the electron thermal velocity (v_{te}), instability can arise if the electron temperature T_e substantially exceeds the ion temperature T_i [1]; it is then called “ion acoustic instability” [2, section 9.7]. When, instead, $v_{de} \gtrsim v_{te}$ the usually more rapidly growing instability is called the “Buneman instability” in recognition of its earliest investigator. Buneman himself initially [3] addressed situations when the ion temperature was negligible, but it is known that the instability occurs for a wide range of temperature ratios [4], including $T_i/T_e > 1$.

Buneman unstable waves easily grow to amplitudes where nonlinear effects, such as particle trapping, saturation, and turbulence, become dominant. And analytic investigations of the nonlinear state have been pursued for many years, often based on Fourier treatments in terms of wave number and frequency, extending[5] the linearized eigenmode analysis, and often invoking quasi-linear assumptions [6]. The purpose of the present discussion is to address

a complementary viewpoint on the nonlinear plasma state, namely the identification of localized potential structures that act as persistent and approximately independent entities. Ion acoustic *solitons*[7] are generally treated through fluid equations, and in addition to having fixed amplitude-speed relations, pass through one another with minimal interaction. However, the more general collisionless kinetic BGK structures[8] can have regions of phase-space with depleted particle density and are hence often called electron or ion *holes*. Holes are of particular interest since they can persist self-consistently but also interact strongly with one another and with solitons[9–14]. Solitary potential structures are now observed widely in space plasmas, yet the processes by which they are formed are themselves rarely observable. One important open question, addressed here, is whether, and under what circumstances, Buneman instability produces electron or ion holes, and what distinctive character those Buneman-produced structures might have. We shall see that the answer is complicated.

Numerical simulation is particularly revealing of the formation and dynamics of localized and solitary potential structures. For Buneman instability, past simulations have been broadly of three types: (a) initialized with a pre-existing velocity drift without applied electric field, usually in a periodic domain, [15–18] (b) applying a fixed current in an open domain [14, 19–21], (c) applying a fixed external field driving increasing current until instability develops [22–27]. The approaches (b) and (c) are particularly appropriate for investigating “anomalous resistivity” arising from the nonlinear turbulence whose level can continue to grow past initial saturation. Approach (a) effectively prescribes the free energy available for the nonlinear state which allows its spatial average to become steady. Case (a) is the focus of the present work, of which a major novelty is the construction of videos of high-resolution phase-space density evolution extending thousands of electron plasma periods into the saturated nonlinear state.

It is known from both observation and simulation that potential variation in multiple dimensions is important, especially for driven electric current. For example, instabilities propagating obliquely with respect to the magnetic field are probably responsible for producing holes of limited transverse extent, and lower hybrid waves, for example, may perhaps disrupt the continued electron runaway in electric-field driven situations. Nevertheless, the present simulations are one-dimensional. The main reasons for this choice include that the computational burden of multidimensional simulations reduces the parameter ranges that can reasonably be studied, and often compels the adoption of unphysical parameters such as ion/electron mass ratio which certainly strongly affects nonlinear development. But also, the difficulty of diagnosing and visualizing the phase-space behavior becomes very much greater in multiple dimensions. The resulting multi-dimensional time-dependent complexity is then not readily susceptible to rendering in the form of (two-dimensional) videos, which is the present emphasis. One must nevertheless be conscious that multi-dimensional effects are deliberately being excluded here, and yet in many situations they may be vital for a complete understanding of the phenomena.

The bulk of the text of this article aims to describe what is observed to occur in the videos referred to. Figures consisting of overall contour summaries and phase-space snapshots are inserted for orientation and illustration, but are not intended to show everything that is observed and described. Analytic theory of steady nonlinear waves aimed at modelling the structures observed is developed, and seems consistent with some early features of the simulations when the electron distributions are not greatly modified, and the structures are

approximately steady in some propagation frame. But the analysis makes major simplifying approximations and should be considered a qualitative interpretive frame-work, rather than a precise representation.

2 Simulations

The present simulations use the (well validated) COPTIC (3-D) electrostatic (PIC) particle in cell code[28, 29], but limited to one spatial dimension x . It solves the Vlasov-Poisson system by implementing on a potential grid the dynamics of two particle species, j . Its units are normalized to the relevant plasma scales, so the governing equations are

$$\frac{\partial f_j}{\partial t} + v \frac{\partial f_j}{\partial x} - q_j \frac{m_e}{m_j} \frac{\partial \phi}{\partial x} \frac{\partial f_j}{\partial v} = 0, \quad \frac{\partial^2 \phi}{\partial x^2} = - \sum_{j=e,i} q_j n_j. \quad (1)$$

The units of time are $\omega_{pe}^{-1} = (ne^2/\epsilon_0 m_e)^{-1/2}$. Space units are $\lambda_{De} = v_{te}/\omega_{pe}$, defined using the initial electron temperature T_{e0} , which sets the energy units. The velocity units are then $v_{te} = \sqrt{T_{e0}/m_e}$ and charge units e , so $q_j = \pm 1$. A total of typically 16 million each of pseudo-particle electrons and ions, $m_i/m_e = 1836$, is used, in a periodic domain of length $L = 255\lambda_{De}$, which permits typically dozens of Buneman wavelengths. Periodicity models a more extended plasma region, but imposes distant correlations that probably somewhat affect the details of behavior in the nonlinear phase. Cell size $\Delta x = 1\lambda_{De}$ and timestep $\Delta t = 0.5\omega_{pe}^{-1}$ give sufficient resolution, as verified by tests using higher resolution that reproduce the results. Of course, the PIC particles are distributed across a continuum of velocities and positions. They are initially loaded with uniform Maxwellian distributions, the ions having zero velocity shift and the electron Maxwellian shifted by v_{de} using a randomized “quiet start” algorithm to suppress initial long-wavelength noise. Diagnostics accumulate their phase-space density at time intervals down to Δt , as two-dimensional histograms having 50 equal velocity intervals, and 200 equal space intervals. Velocity integrals provide electron and ion density $n_j(x, t) = \int f_j dv$, whose initial values are normalized to unity. The potential, $\phi(x, t)$, provides the electric field $E = -\partial\phi/\partial x$, and allows average electric field energy density $\langle E^2 \rangle = \int E(x, t)^2 dx/L$ to be integrated. A parallel magnetic field does not affect the one-dimensional dynamics, which is considered parallel to any B .

3 Time-dependence Contour Summaries

Figure 1 shows how the long-term nonlinear time development of Buneman instabilities depends on the ion temperature. With constant initial electron velocity shift ($-2v_{te}$), for cold ions (a) $T_{i0} = 0.04(\times T_{e0})$, the initial sinusoidal unstable wave(s) have speed slightly exceeding the cold ion sound speed $c_s = \sqrt{T_{e0}/m_i}$ propagating (relative to ions) in the same (negative) direction as the electron distribution shift. As the potential perturbations approach unity amplitude (and energy saturation) however, they accelerate. This acceleration might be caused partially by the spreading of the electron distribution, but also as will be shown later, higher phase speeds are associated with greater potential amplitude and longer wavelengths. The highest potential peaks ψ have electron holes trapped within the ion perturbations whose

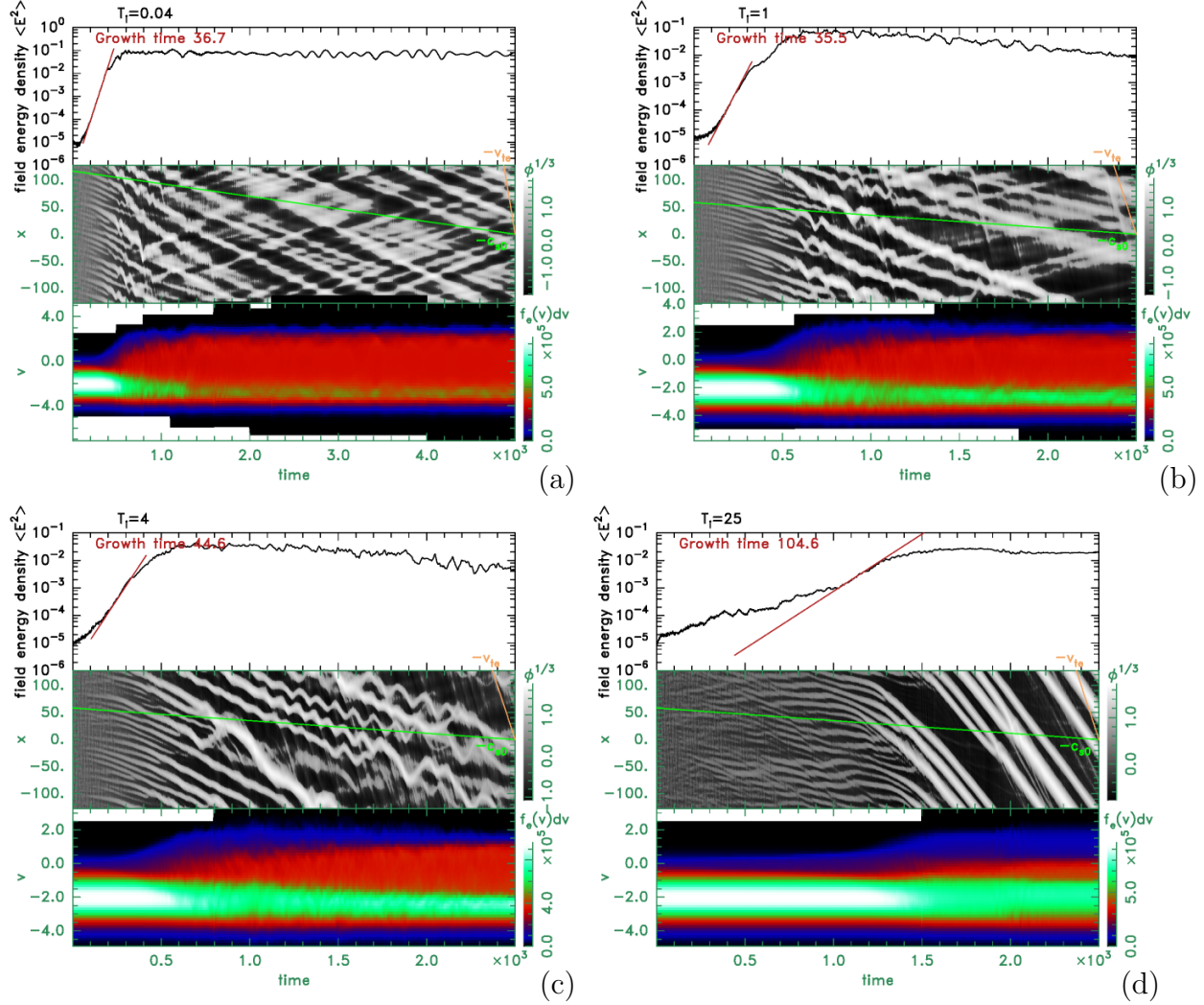


Figure 1: Four summaries showing time-dependence of 1-D periodic PIC simulations of nonlinear Buneman instability growth with initial Maxwellian electrons of velocity shift -2 (units of $\sqrt{T_{e0}/m_e}$), and (unshifted) initial ion temperatures (relative to electron) $T_{i0} =$ (a) 0.04, (b) 1, (c) 4, (d) 25. Top panels: electric field energy-density. Middle panels: cube root (to expand dynamic range near zero) potential $(\phi(t, x))^{1/3}$ contours. Bottom panels: spatially averaged electron distribution function contours of the total number of simulation-particles in velocity range dv ; i.e. $f_e(t, v_e)dv = dv \int_L f_e(t, x, v_e)dx$, where dv is the velocity width of a single histogram box, equal to the initial total velocity range divided by 50 and L is the total domain length.

signature is rapid oscillation of the peak position, observable in Fig. 1 during $t \sim 500-1000$ (units of ω_{pe}^{-1}), with oscillation speeds a substantial fraction of electron thermal speed. The speed of the structures averaged over oscillations is typically up to $6c_s$. The oscillations appear to generate positive-propagating peaks after about $t = 800$, giving rise to diagonal cross-hatching of the potential contour plot, which persists thereafter. The potential peaks move at $\sim \pm 3c_s$ in this later phase ($t \gtrsim 3000$).

When (b) $T_{i0} = 1$ the behavior is fairly similar, though with fewer positive-propagating peaks being generated. But when (c) $T_{i0} = 4$, there are hardly any positive-propagating peaks, and the oscillatory behavior persists throughout, with the number of distinct peaks gradually decreasing through mergers; their speeds remain higher: $\sim 6c_s$. In addition in (b) and (c) there are much thinner, steeper, mostly downward streaks at near electron thermal speed, which detailed phase-space portraits show to be mostly small electron holes spawned near larger vortex separatrices.

When (d) $T_{i0} = 25$, the initial perturbation growth is very slow, and short wavelength waves moving at near the acoustic speed dominate until time 1000. The growth time fitted line in this case does not correspond to a linear phase. Instead its algorithm chooses the following period when the wave peaks simultaneously grow, accelerate, and merge, so that by 1500 the field energy saturates at close to the lower- T_{i0} cases' levels, and is concentrated in just three potential peaks by 2200. These are clearly electron holes, traveling at (minus) almost half the initial electron thermal speed (relative to ions), approximately $18c_s$. In this case, the average electron distribution function has been broadened only in a limited velocity extent around zero, unlike the low- T_{i0} cases which show flattening over much of the final f_e spread.

4 Phase Space Dynamics Videos

4.1 Velocity shift $v_{de} = 2$

The full phase-space of the simulations summarized in Figure 1 is imaged as a function of time in videos of which the contour plots Figures 2, 3 and 4 are individual frames. These videos add persuasive phase-space portraits to enable the dominant time-dependent phenomena to be identified.

Case (a) $T_{i0} = 1/25$, whose video can be viewed at <https://youtu.be/1Sc8Z1hoYas>, and of which Fig. 2 is a frame, shows rapid early growth of an unstable wave, large enough by time 200 to trap electrons and form vortices in the electron phase-space. Velocity units are initial electron thermal velocities for both panels. The contour units of f are the number at this time step of simulation particles per pixel of the phase-space, thus giving a measure of statistical uncertainty. Where indicated, the base-10 logarithm of f_i is contoured to reveal small-amplitude structure. Spatially averaged initial and instantaneous velocity distributions, rescaled to constant peak height, are shown at right. Time of frame is printed top right. Adjacent potential peaks merge with each other so that the electron (species 1) vortices along with their associated ion velocity perturbations grow larger and fewer. By $t=500$ the number of vortices is about half its initial number, and the largest potential peak has reached 2. By 750 another approximate halving of the vortex numbers has occurred with

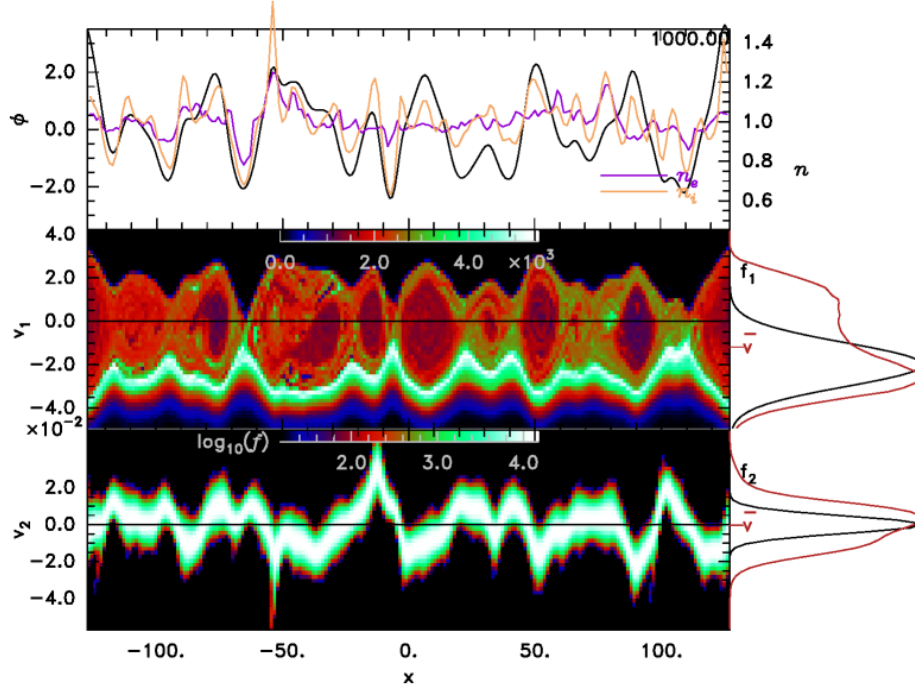


Figure 2: Example frame of video for $T_{i0} = 0.04$ (case (d)), showing top: potential, and electron and ion densities; middle: electron phase-space density f_e contours; bottom: ion phase-space contours.

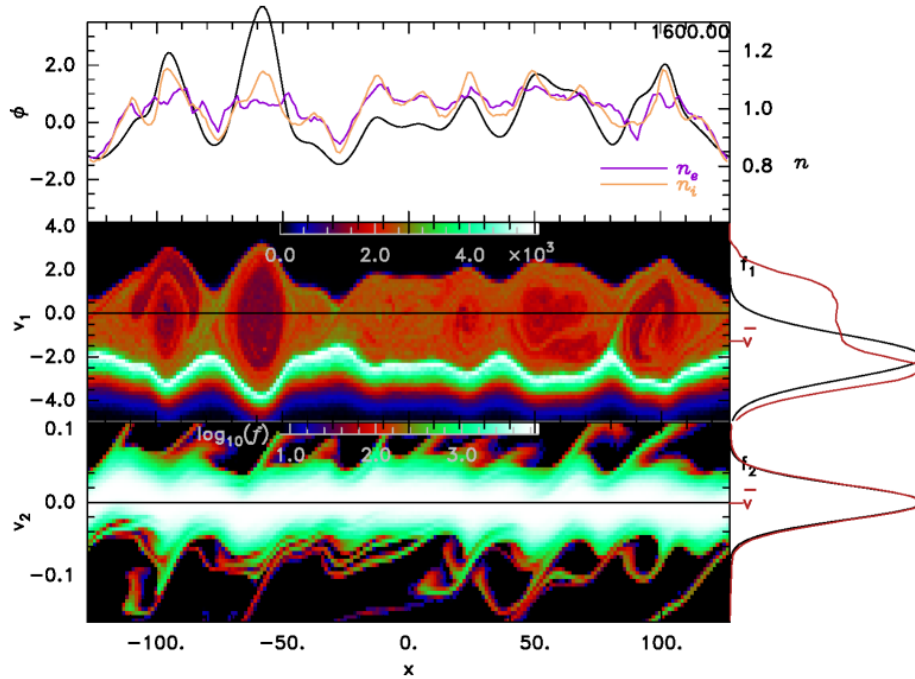


Figure 3: Phase-space ion streams for case (b) $T_{i0} = T_{e0}$ are observed as filaments in the region $|v_2| \gtrsim 0.5$ in the f_2 contour plot (logarithmic for greater resolution of low values). They coincide with the positive peaks of ion density and potential.

peak potentials up to 4. The electron and ion density perturbations at this stage are of comparable magnitude and no longer in antiphase as they had been during most of time till 400. Merging into discrete vortices has mostly stopped by time 1000 and thereafter the ion and electron densities, and potential perturbations are all in phase, but with the ion perturbation amplitude exceeding the electron. The trapped phase-space f_e depression of the electrons is only a modest contributor to potential perturbations. The electron vortices continue to merge and divide under the dominant influence of ion density fluctuations. To call them electron holes in these late stages would be misleading, considering their minimal electron phase-space depletion.

Case (b) $T_{i0} = 1$, viewable at <https://youtu.be/-LcFx--4SgE> (and with f_2 contoured linearly at <https://youtu.be/USz-k3gEBUG>) is largely similar, but the substantial initial ion velocity spread $T_{i0} = T_{e0}$ allows the formation of spatially-localized high speed filamentary ion streams accelerated to both positive and negative velocities, which then move (and shear) in accordance with their phase-space positions in both positive and negative directions. Figure 3 shows a frame. The ion density enhancements are then greatest where both positive and negative velocity streams are present at the same position, that is at the intersection of the opposite slope diagonal lines in Figures 1(a) and (b). Again, ions dominate the longer term potential fluctuations, and electron vortices bounce around under the ions' influence.

Case (c) $T_{i0} = 4$, viewable at <https://youtu.be/K-3p7rprikY> shows greater persistence of the electron vortex structures. They bounce around quite rapidly in the background ion density perturbations, but the relative importance of ion contribution to potential is lower, because the higher ion temperature phase-mixes f_i perturbations more rapidly. The electron vortices that remain, toward the end of the simulations, still have substantial f_e and n_e depression, and self-identity, even though their buffeting by the ions causes them to decay in magnitude (and number) fairly rapidly. The final average electron distribution is far less flattened than before.

Case (d) $T_{i0} = 25$, viewable at <https://youtu.be/pawoTH5rGUQ>, and of which Fig. 4 is a single frame, takes a long time for the instability to grow to a level where nonlinear effects are obvious. Its initial wavelength is considerably longer. The spurt of energy growth starting at $t=1000$ accompanies a group of peaks that accelerate (in the negative direction) rapidly and devour the smaller, slower peaks; so that by 1500 only five peaks with their vortices are left, all moving fast. Two further merges occur so that by 2200 only three peaks remain; see Figure 4. These are very obviously persistent electron holes for which the ion density perturbation influence is small, in part because of the high ion temperature, but also because the holes move much faster than the ion thermal speed, also reducing the ion response. The final distortion of the electron average distribution f_1 appears mostly as two regions of reduced gradient, attributable to the holes themselves, and not the background between them.

4.2 Larger velocity shift

When the distribution shift is greater ($3v_{te}$), the $T_{i0} = 25$ case is illustrated in Figure 5 and viewable at <https://youtu.be/G2GZgww-87Y>. The initial growth is no longer significantly slowed. However, like the corresponding $2v_{te}$ shift case, strong acceleration of the potential peaks accompanies saturation, leading to electron hole merger, and finally by time 1500 to a

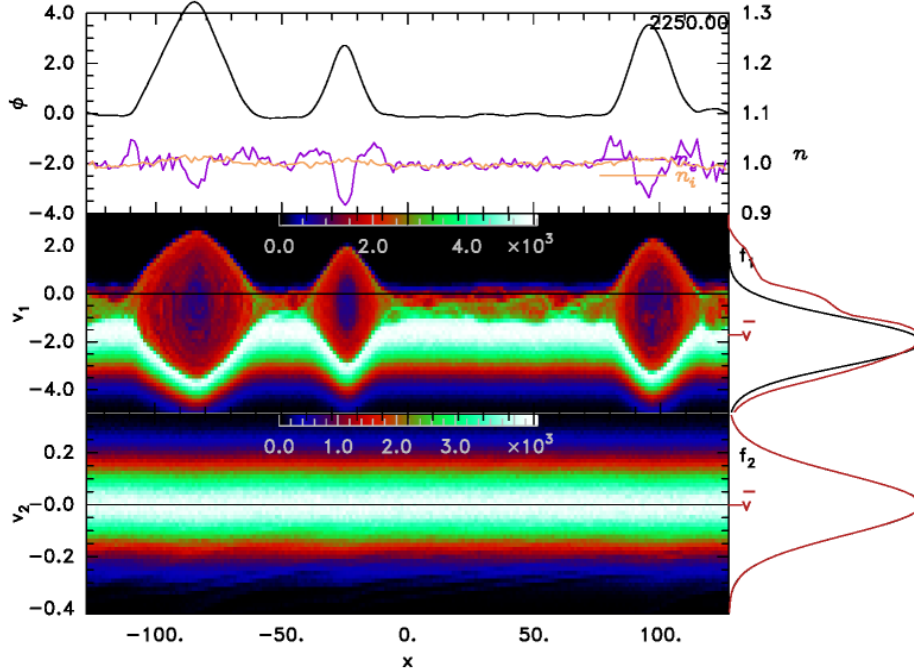


Figure 4: The fully developed phase-space of case (d) $T_{i0} = 25$. High ion temperature leads to fast moving accelerated electron holes, and only minor background distribution perturbations.

rapidly moving single hole with large amplitude $\psi \sim 8$. It experiences occasional reflections from the potential perturbations produced by slowly evolving ion density perturbations, but persists beyond time 5000 with only gradual diminution of its amplitude caused mostly by detrapping associated with the reflections. The background electron velocity distribution is extensively flattened, but the spatially averaged ion distribution is only weakly perturbed.

For $v_{de} = 3$ and $T = 1$, (video at <https://youtu.be/yL3jLr1br4k>) the initial growth time is extremely fast, only 14, and by time 1000 electron holes have mostly dissipated during a period of high perturbation amplitude $\psi \sim 10$, leaving counter-propagating ion-generated potential peaks with speed $\sim 6c_s$, together with extended ion phase-space streams, and $\psi \sim 5$ by time 2500.

4.3 Smaller velocity shift

Figures 6, 7, and 8 illustrate cases with smaller velocity shifts v_{de} of the initial electron distribution. When $v_{de} = -1.3$ (and $T_{i0} = 1$), which can be considered at the threshold[30] of equal-temperature Buneman instability, (Fig. 6(a) video at <https://youtu.be/WpRx-5CUzZ8>), the potential perturbation grows weakly with modestly accelerating peaks, and the total field energy saturates at a low level. Even during this early phase the electron and ion density perturbations are of comparable magnitude. Then the peaks merge, increasing their height to $\psi \simeq 0.15$ without significant total field energy growth, and accelerate somewhat more. Ion and electron density perturbations are of comparable amplitude, both positive at the potential peaks, with modest trapped f_e depression. By time 4400 only five peaks are left

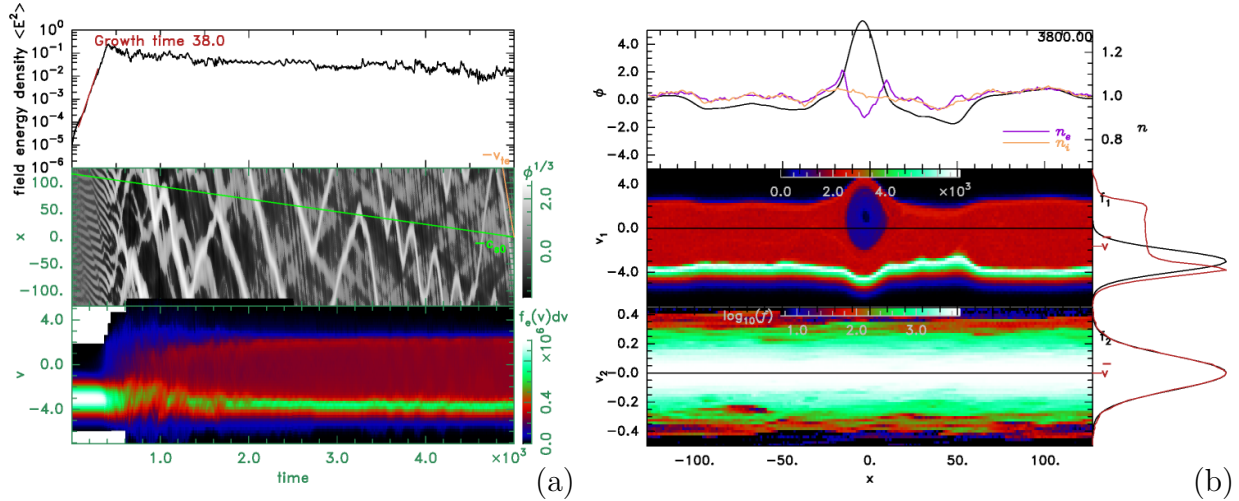


Figure 5: Results with high $T_{i0} = 25$ and greater initial distribution shift $3v_{te}$. (a) Time evolution; (b) snapshot of final electron hole.

and merging has become rare. A (barely detectable) narrow region of reduced slope at zero velocity is present on the spatially averaged f_e . The peaks' speed, $\sim -4c_s$, can probably be interpreted as approximately the nonlinear ion acoustic speed for the corresponding shifted electron distribution as will be discussed later. A simulation Fig. 6(b) (video at <https://youtu.be/fwLCVTGD6ZE>) with lower ion temperature $v_{de} = -1.3$, $T_{i0} = 0.04$ reaches considerably higher field energy density ($\sim 3 \times 10^{-3}$) and peak potential ~ 0.8 . Its potential peaks are on average slower than those of Fig. 6(a). They also have oscillating coupled electron holes, which sometimes temporarily escape the ion density perturbations. In neither case is a clear linear growth fit of the early stages persuasive.

The intermediate velocity $v_{de} = -1.5$, $T_{i0} = 1$ case (Figure 7, video at <https://youtu.be/ThRDFiP4FFo> and a shorter linear f_i -contours version at <https://youtu.be/701J814aUr>) has no substantial early electron hole oscillations and has weak average f_e perturbations and final peak heights $\psi \simeq 0.8$, after substantial mergers over times of several thousand ω_{pe}^{-1} . The potential in the early nonlinear stages is generated approximately equally by opposite polarity electron and ion density perturbations, giving what can be considered a train of electron holes coupled steadily to soliton-like ion density modulations. However as peak mergers raise their amplitude and speed, the electron phase space, Fig. 7(b), shows that the electron density is actually somewhat greater in the potential peaks than outside, and there is only weak depletion of f_e in the trapped region. The ion density enhancement is greater (sustaining the potential peak) and arises mostly from local expansions of the ion distribution toward negative velocities, accompanied by some ion streams. Thus these very long-lived structures have a mostly soliton character but their speed, $\sim 4.5c_s$, is enhanced by the substantial electron distribution shift, as will be analysed later. It is notable in the video that each merging process consists of a larger amplitude peak overtaking a smaller amplitude peak. That is consistent with soliton speed increasing with amplitude. However, merging is not consistent with historic analysis of KdV fluid solitons, which pass through one another and emerge with their identities and amplitudes intact. Thus, again, these solitary waves

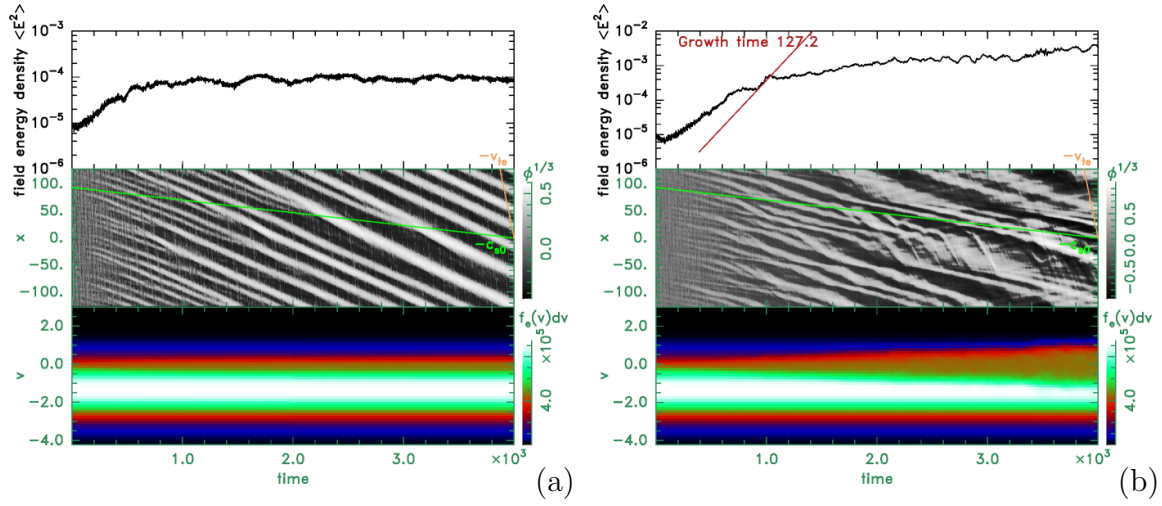


Figure 6: Nonlinear summaries for shift velocity $v_{de} = -1.3$, near the Buneman stability threshold. (a) $T_{i0} = 1$, (b) $T_{i0} = 0.04$. Corresponding videos are at (a) <https://youtu.be/WpRx-5CUzZ8>

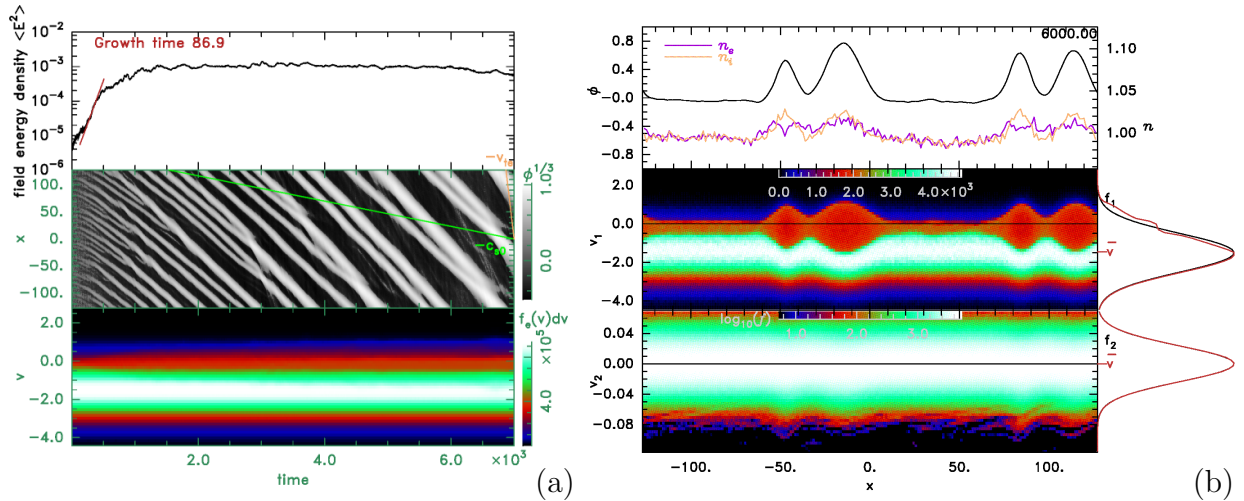


Figure 7: (a) Contour summary, (b) phase-space snapshot at time 6000, of simulation with $v_{de} = -1.5$, $T_{i0} = 1$.

should probably be thought of as CHS structures where the trapped electron dynamics is important.

For this shift, $v_{de} = -1.5$, lowering T_{i0} to 0.04 (video at <https://youtu.be/75MhqpX0djE> and shorter linear f_i -contour version at https://youtu.be/_MHqEAPYTzE) raises the peak amplitude to $\psi \sim 2$, from which it later relaxes to ~ 1 , restores coupled electron hole oscillations, substantially widens the f_e , produces a few long fast ion streams which emerge from high electric field regions, and produces occasional streams of electron holes that are rapidly captured and usually dissipated.

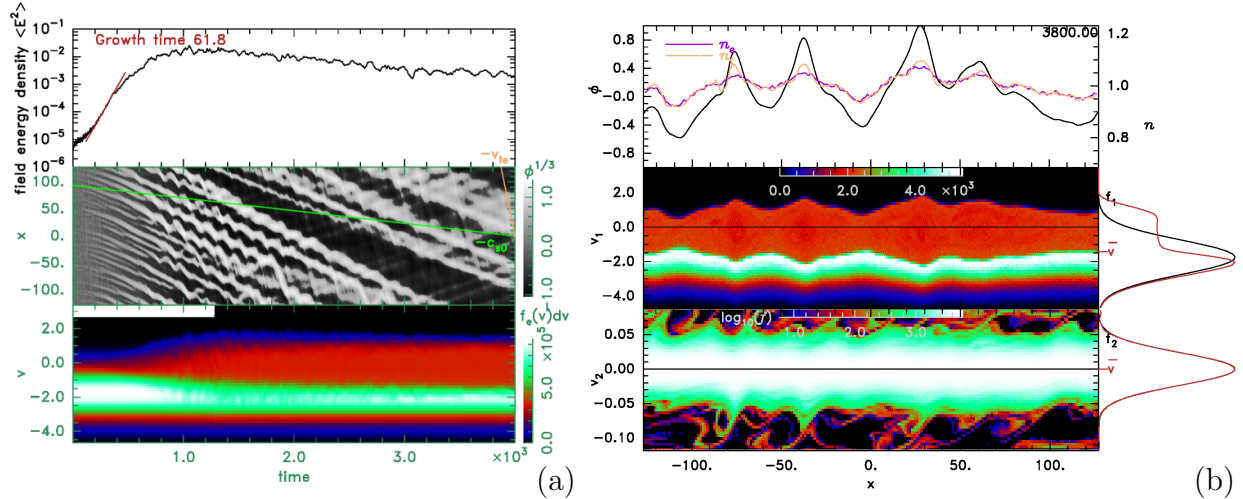


Figure 8: (a) Contour summary, (b) phase-space snap shot, when $v_{de} = -1.75$, $T_{i0} = 1$.

Figure 8 has $v_{de} = -1.75$, $T_{i0} = T_{e0}$ (video https://youtu.be/_xFMa-8cWHY, linear at <https://youtu.be/97wzpGqSCVo>). It is similar to the corresponding $v_{de} = -2$ case except that none of the forward-propagating ion structures are of clear CHS structure. Instead the faint cross-hatching in Fig. 8(a) appears to be caused by the high speed ion streams of positive velocity. It has a substantially flattened f_e and the potential peaks approach $\psi \simeq 2$ at time 1000, with deep trapped f_e depressions and negative n_e excursions. These are electron holes trapped but unstable in CHS phenomena, and their average negative speed is $\sim 5c_s$. Thereafter the peaks gradually decay to $\psi \sim 0.8$ by time 4000, as the trapped electrons are phase-mixed and the trapped f_e depressions are smoothed away, with the result shown in Fig. 8(b).

At this $v_{de} = 1.75$, but with high ion temperature $T_{i0} = 25T_{e0}$, the video at <https://youtu.be/wUnVmEBEJ7A> shows formation of electron phase-space vortices, merging to give larger electron holes (up to $\psi = 2.7$) with noticeable central f_e -depression, and moving at high speed ($v_p \sim 20c_s$, very similar to the high- T_{i0} , $v_{de} = 2$ case of figure 4).

4.4 Phenomenological summary

When $|v_{de}| > 1.5$, high $T_{i0} \gg T_{e0}$ favors formation of electron holes that are accelerated to speeds much greater than the ion thermal and sound speeds. When the free energy released by the instability is high, they are occasionally reflected from ion perturbations, but without

being trapped by a coherent ion density peak. More moderate temperature ratios $T_{i0} \lesssim 4T_{e0}$ allow soliton-like ion perturbations to trap electron holes within themselves, forming coupled hole-solitons (CHS), often with hole oscillations. At ion temperatures $T_{i0} \lesssim 1$ the CHS structures mostly disassemble by approximately time 1000, giving rise to counter-propagating individual potential peaks attributable to ion density perturbations moving at speeds several times $\sqrt{T_{e0}/m_i}$.

Higher distribution shifts ($v_{de} = -3$) give rise to higher potential peaks, and produce ion fluctuations that, even at $T_{i0} = 25$, are large enough to reflect the electron holes.

Lower distribution shifts decrease the peak potential height, avoid generating forward-propagating structures, and reduce the f_e flattening. Their potential peaks have speeds of order $4c_s$ showing they are neither pure electron holes nor standard ion acoustic solitons.

No obvious *ion holes*: ion phase-space vortex structures in negative polarity potential valleys, have been observed in any case. Instead, influential ion streams in phase-space are generated when the potential peaks are high enough, and initial ion temperature is ~ 1 or 4. The streams extend to speeds $|v_i|$ several times v_{ti} , but remain relatively incoherent, becoming turbulently randomized or elongated, preventing a coherent ion vortex from being completed.

5 Analytic Structures

The purpose of this section is to present a highly idealized analysis based on adopting model electron and ion distributions that are a function only of energy, in a frame of reference in which the steady potential form is stationary: hence satisfying Vlasov's equation. Certain constraints and relationships between the distribution and the potential structure's velocity relative to them emerge from calculation of the resulting self-consistent potential shape $\phi(x)$. The analysis here parallels the treatment of [31, 32], but avoids small-argument expansion of $n(\phi)$, and directly calculates wavelength and spatial profile numerically, based on a specific choice of distribution shapes. The advantage for present purposes is more transparent algebra, and comprehensive quantitative results. However, it does not take account of variable phase-space depletion of trapped electrons; so the approach can be considered a kind of fluid analysis, rather than a treatment appropriate for electron or ion holes.

The model distribution of ions is, for algebraic simplicity, a single velocity stream (cold plasma fluid) whose speed v in the potential structure's rest frame is given by constant energy $\mathcal{E} = \frac{1}{2}mv^2 + q\phi = \text{const}$. In dimensionless units, the stream velocity is then $\sqrt{2(\mathcal{E}_i - \phi)/m_i} = \sqrt{2(\mathcal{E}_i - \phi)}c_s$ (since $T_{e0} = 1$). Adopting the ion speed at zero potential as the primary reference (to a good approximation the initial simulation ion velocity), the structure (phase) velocity in the ion frame is $v_p = \sqrt{2\mathcal{E}_i}$. The sign of v_p and of v_{de} is taken positive in this analysis section to avoid frequent minus signs. The (assumed steady) ion density is then $n_i(\phi) = n_i(0)/\sqrt{1 - \phi/\mathcal{E}_i}$, valid only as long as there is no ion reflection ($\phi_{max} \equiv \psi < \mathcal{E}_i$).

The electron distribution $f_{ep}(v_e)$ in the structure frame of reference for untrapped (passing) particles, $\mathcal{E}_e = v_e^2/2 - \phi > \phi_{min} = 0$, is taken as a Maxwellian of temperature $T_{e0}(= 1)$, shifted from the ions by a drift velocity v_{de} . Their drift velocity relative to the potential structure frame is then $v_{de} - v_p$ and $f_{ep} = \exp[-(v_e - v_{de} + v_p)^2/2]/\sqrt{2\pi}$. In this hypothetical steady state, trapped electrons must have a symmetric distribution, and are taken to have

a distribution function independent of velocity: $f_e(\mathcal{E}_e < 0) = f_{ep}(\mathcal{E}_e = 0)$. This form of distribution is called flat-trapped. The corresponding density $n_e(\phi)$ cannot be expressed compactly through standard functions but can quickly be numerically evaluated and has been plotted elsewhere[12, figure 10]. Electron holes have trapped distribution *deficit* relative to flat-trapped. But many of the electron vortices observed in the videos have small deficit; so adopting flat-trapped electrons is reasonable approximation, even though often only a fairly crude one. We are not here addressing the structure of the observed electron holes, but of the wave peaks arising from electron-ion interactions.

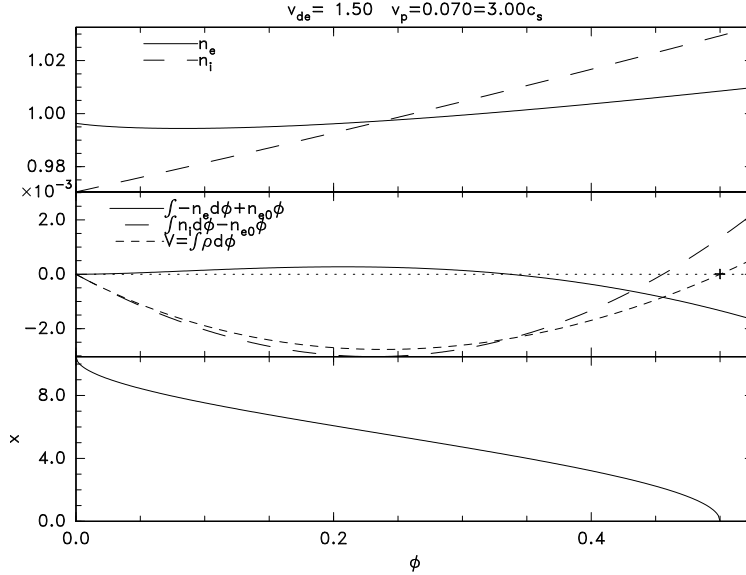


Figure 9: Illustration of the pseudo-potential analysis.

Figure 9 illustrates the solution process of the resulting Vlasov-Poisson system, with electron shift $v_{de} = 1.5$, structure phase velocity $v_p = 3c_s$ (both in the ion frame), and peak height $\psi = 0.5$ (relative to $\phi_{min} = 0$). These parameters give the corresponding $n_e(\phi)$ and $n_i(\phi)$ shown in the top panel. The self-consistent solution of Poisson's equation can be found by obtaining the first integral $-\frac{1}{2} \left(\frac{d\phi}{dx}\right)^2 = V(\phi) = \int_{\phi_{min}}^{\phi} q_i n_i + q_e n_e d\phi$, which is called the pseudo-potential. It is shown in the middle panel together with the contributions of electrons $\int -n_e(\phi)d\phi + n_{e0}\phi$, and ions $\int n_i(\phi)d\phi - n_{e0}\phi$ (using shorthand notation $n_0 \equiv n(\phi_{min})$), in which the addition and subtraction of $n_{e0}\phi$ serves to enable plotting on a convenient scale. The sum of the electron and ion contributions is the pseudo-potential $V = \int \rho d\phi$. It must be negative over the potential range (whose upper end is $\phi_{max} = \psi$ where $V = 0$), to ensure $d\phi/dx$ is real. Then the potential variation with position is found implicitly from $\int_{x_{min}}^x dx = \int_{\phi_{min}}^{\phi} d\phi/\sqrt{-2V}$ shown in the bottom panel. This procedure is familiar in the analysis of solitons and electron-holes (see for example [12, 33, 34]), where truly solitary structures require that the second derivative of ϕ which is proportional to the charge density, becomes zero at ϕ_{min} : $n_{e0} = n_{i0}$. However, the present context includes approximately periodic (wave-like) structures. For finite wavelength, no such second derivative requirement arises. Instead all that is formally required is that the total charge contained in a half-period be zero: $V(\phi_{max}) = V(\phi_{min}) = 0$. The wave is no longer quasi-neutral at ϕ_{min} , and instead

we require $n_{e0} > n_{i0}$ to enforce $\frac{d^2\phi}{dx^2}|_{\phi_{min}} > 0$.

Given the velocity distribution shapes, we can construct normalized electron and ion contributions $\hat{V}_e = \int_{\phi_{min}}^{\phi} q_e \hat{n}_e d\phi$ and $\hat{V}_i = \int_{\phi_{min}}^{\phi} q_i \hat{n}_i d\phi$, where $\hat{n} \equiv n/n_0$. The requirement $V = 0$ at ϕ_{max} is

$$n_{e0} \hat{V}_e(\phi_{max}) + n_{i0} \hat{V}_i(\phi_{max}) = 0. \quad (2)$$

If $|\hat{V}_i(\phi_{max})/\hat{V}_e(\phi_{max})| > 1$, then from this equation we can determine n_{e0} and n_{i0} (both positive) such that $n_{e0}/n_{i0} > 1$. Initially it is convenient to take $n_{e0} = 1$. But during the final numerical integration to obtain $x(\phi)$ it is straightforward to calculate the resulting spatially averaged density $\langle n \rangle$. Afterwards one can simply divide n_{e0} , n_{i0} , V_e , and V_i by $\langle n \rangle$ and multiply $x(\phi)$ by $\sqrt{\langle n \rangle}$, to represent a case where $\langle n \rangle = 1$. That has been done for figures 9 and 11(a).¹

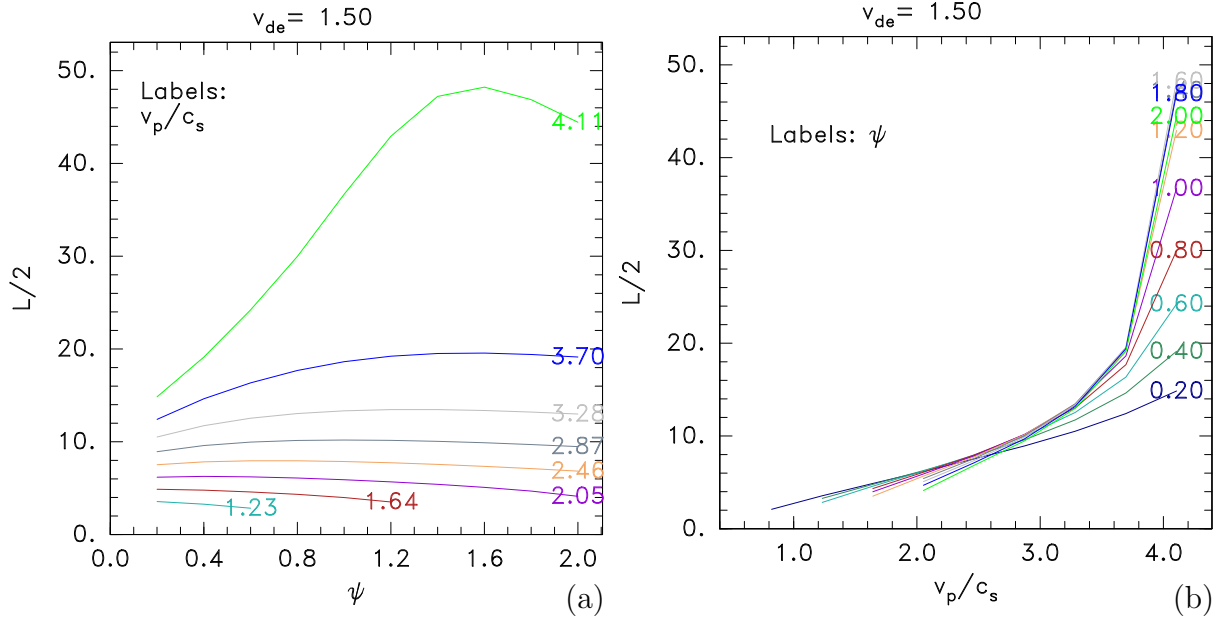


Figure 10: Hole length versus ψ (a) and v_p (b).

For chosen electron and ion distributions, there is generally no guarantee that V remains negative between ϕ_{min} and any chosen ϕ_{max} . If it does not, no valid solution for that ϕ_{max} exists; but valid solutions with small enough ϕ_{max} do exist provided $d\hat{n}_i/d\phi > d\hat{n}_e/d\phi$ at ϕ_{min} and there exists some positive potential at which $\hat{V}_e + \hat{V}_i = 0$. The top panel of figure 9 shows the electron and ion densities determined by the requirement that $V(\psi) = 0$ with $\psi \equiv \phi_{max} = 0.5$, which needs $n_{i0} = 0.974n_{e0}$. The lowest panel is the resulting spatial dependence of the potential for half a wavelength, in which the ordinate is the position x relative to the potential peak. The periodic structure's wavelength is $L = 2 \times 10.5 = 21$ (Debye-lengths) in this case.

¹It has been noted recently, e.g. in [36] and references therein, that pseudo-potential treatments like this (though with $v_{de} = 0$) of nonlinear ion acoustic waves have often ignored the fact that $\langle n \rangle$ is not exactly equal to the reference density that has been used to define the length scale λ_{De} . However, since the treatment here in terms of the normalized \hat{V} shows that the absolute density does not enter into the determination of $\phi_{max} - \phi_{min}$, it is clear that any discrepancy amounts only to a straightforward adjustment of the length (and time) scaling.

The range of half wavelengths ($L/2$) for a specified electron velocity shift obtained by running the solver for many ψ and v_p values is shown in Figure 10. For this electron drift speed (1.5) we see that the wavelength L increases as v_p increases, with gradient increasing as ψ increases. This behavior is consistent with the PIC simulation observations of simultaneous acceleration, peak-potential growth, and wavelength growth. Remember, though, that this theory does not account for the coupled electron hole effects that are observed in the simulations. Phase velocities exceeding about $4c_s$ are prevented for $v_{de} = 1.5$ by the reduction of the ion response, and strong wavelength growth, for $\psi > 1$. These are attributable to reduction of $dn_i/d\phi$ toward $dn_e/d\phi$ eventually preventing the positive crossing of their densities. It should be remarked that these large wavelengths have minima narrower than their maxima. In other words, in the limit they tend to solitary *negative potential valleys*, rather than solitary peaks.

Increasing to $v_{de} = 2$ gives rise to a noticeably negative electron density gradient $dn_e/d\phi$, and permits flatter ion response and higher v_p and ψ as illustrated in Fig. 11. The analytic

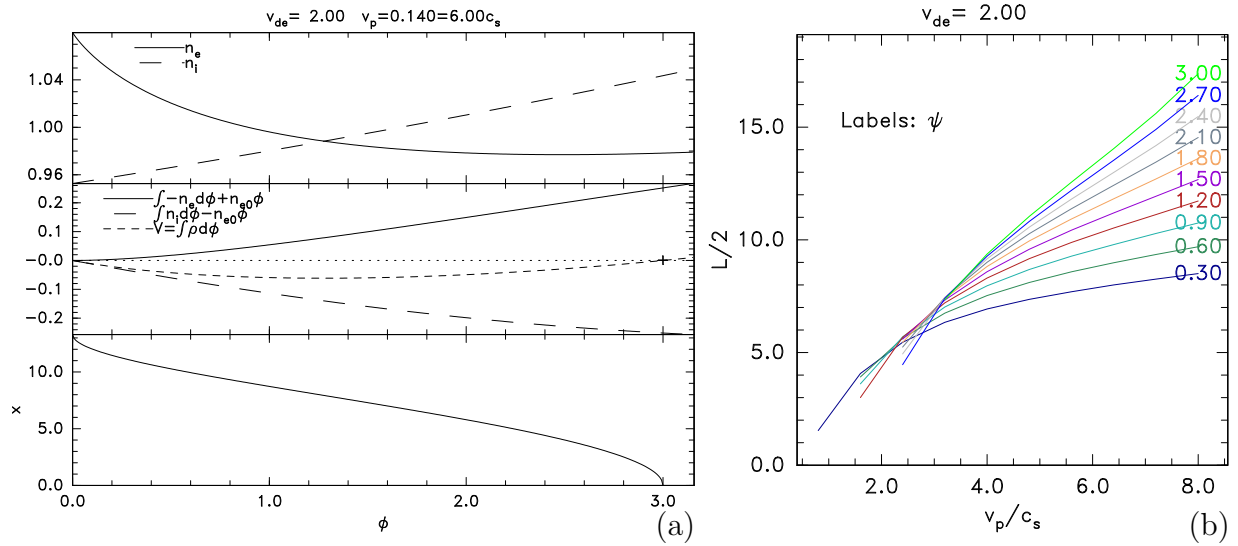


Figure 11: Analytic solutions for $v_{de} = 2$. (a) Solution details. (b) Resulting half-wavelengths for a range of ψ and v_p .

treatment then permits simultaneous growth of v_p , as well as ψ and L , as has been seen in the corresponding simulations. However, the electron density dependence on potential for these analytic structures has $dn_e/d\phi$ negative. Early times in the corresponding simulations do have negative n_e valleys at the potential peaks, but later, when the spatially averaged f_e has an extended flat region, the electron density perturbations reverse their polarity with respect to the potential, and disagree with the analytic predictions. This is presumably because the actual electron distribution has been substantially changed from what the analytic approximation assumes.

6 Discussion

The simulation observations are summarized in a highly simplified form in table 1,

Parameters	Case	a	b	c	d	e	f	g	h	i	j	k	l
	$ v_{de} $	1.3	1.3	1.5	1.5	1.75	1.75	2	2	2	2	3	3
	T_{i0}/T_{e0}	0.04	1	0.04	1	1	25	0.04	1	4	25	1	25
PIC	$e\psi/T_{e0}$	0.8	0.15	2-1	0.8	2-0.8	2.7	2-4	2-4	4	4	10-5	8
observations	$ v_p /c_s$	3	4	3-5	4.5	4.5	20	6-3	4-3	6	18	6	40
Analytic max	v_p/c_s	2.9		4.1		8		16				45	

Table 1: Summary of simulation cases (hyperlinked letter labels), observed structure speed and amplitude, and relevant analytic limit.

which records the observed phase speed of peak propagation $|v_p|/c_s$, and the peak height ψ , arising from different initial simulation parameters $|v_{de}|$ and T_{i0} . It also shows for the corresponding PIC parameters the analytic model’s upper limit of v_p/c_s that permits a solution, which is determined by exploring a range values of v_p . The value of ψ chosen for this exploration changes the limit very little; but the limit is very sensitive to the value of $|v_{de}|$. In particular, there is a very rapid transition in the range $1.5 < |v_{de}| < 1.75$ between a value $\sim 4c_s$ that is of approximately the same magnitude as observed in the simulations, to a much higher analytic upper limit for larger $|v_{de}|$. In short, when $|v_{de}| \leq 1.5$ there is an equilibrium limit to v_p , while for $|v_{de}| > 1.75$ the simulation phase velocity is *not limited* by nonlinear equilibrium, because $dn_e/d\phi$ is negative. The higher $|v_{de}|$ simulations appear to be saturated by the strong electron distribution flattening when the potential exceeds $\sim v_{de}^2$, which is sufficient to make the electron phase-space vortices reach beyond v_{de} . The $T_{i0} = T_{e0}$ simulations of Tavassoli et al [18] observed a threshold for generation of counter-propagating potential peaks they call “backward waves”, between v_{de} values of $1.5c_s$ and $1.75c_s$, which they attributed to the increase of the averaged distribution flattening as the peak potential increases, and the consequent reduction in backward waves’ theoretical linear growth rate in this distribution. The present observations agree, except that we observe the backward waves emerging from coupled electron hole oscillations, so there is more to the story. Clearly, a lot is changing in this range of drift speeds.

Only the high- T_{i0} cases (f), (j) and (l) give predominant electron holes, rather than slower ion-dominant structures. Electron holes of various amplitudes are created in the lower ion temperature cases, but are trapped or reflected by the potentials generated by ion density perturbations. The result is sometimes a quiescent CHS, sometimes an oscillatory CHS, and sometimes buffeting small electron holes incoherently between different potential peaks.

In summary, the nonlinear evolution of perturbations in an initially Buneman unstable one-dimensional plasma, is revealed to have many quasi-coherent features that are not well represented by random-phase quasi-linear analysis, but can be fruitfully (though incompletely) understood in terms of compound entities such as electron holes, coupled hole-solitons, and non-linear wave peaks. These structures move faster relative to the ions than classic ion-acoustic solitons, but with the exception of free electron holes not faster than than about $6c_s$, or even $4.5c_s$ for electron drift speeds less than approximately 1.75 times the electron thermal speed $\sqrt{T_{e0}/m_e}$. Their general trend is that phase speed and spatial period increases with potential height. When such structures are solitary they do not retain their identity when they overtake one another as do KdV solitons. Instead they combine to

form a peak of greater height. Electron holes are generated only when $T_{i0} \gg T_{e0}$. Ion hole formation does not occur.

It is hoped that the easy access to the simulation movies will provoke in other investigators further insights into the nonlinear phases of this classic instability, and the formation of persistent potential structures.

Acknowledgments

This work was not supported by any external funding.

References

- [1] B. D. Fried and R. W. Gould, Longitudinal Ion Oscillations in a Hot Plasma, *The Physics of Fluids* **4**, 139 (1961).
- [2] N. A. Krall and A. W. Trivelpiece, *Principles of Plasma Physics* (McGraw-Hill, 1973).
- [3] O. Buneman, Instability, Turbulence, and Conductivity in Current-Carrying Plasma, *Physical Review Letters* **1**, 8 (1958).
- [4] E. A. Jackson, Drift Instabilities in a Maxwellian Plasma, *The Physics of Fluids* **3**, 786 (1960), https://pubs.aip.org/aip/pfl/article-pdf/3/5/786/12499226/786_1_online.pdf .
- [5] A. A. Galeev, R. Z. Sagdeev, V. D. Shapiro, and V. I. Shevchenko, A nonlinear theory of the Buneman instability, *Zhurnal Eksperimentalnoi i Teoreticheskoi Fiziki* **81**, 572 (1981).
- [6] R. C. Davidson, *Methods in Nonlinear Plasma Theory* (Academic Press, New York, 1972).
- [7] E. Infeld and G. Rowlands, *Nonlinear Waves, Solitons and Chaos*, 2nd ed. (Cambridge University Press, Cambridge, 2000).
- [8] I. B. Bernstein, J. M. Greene, and M. D. Kruskal, Exact nonlinear plasma oscillations, *Physical Review* **108**, 546 (1957).
- [9] K. Saeki, P. Michelsen, H. L. Pecseli, and J. J. Rasmussen, Formation and Coalescence of Electron Solitary Holes, *Physical Review Letters* **42**, 501 (1979).
- [10] K. Saeki and J. J. Rasmussen, Stationary solution of coupled electron hole and ion soliton in a collisionless plasma, *Journal of the Physical Society of Japan* **60**, 735 (1991).
- [11] K. Saeki and H. Genma, Electron-Hole Disruption due to Ion Motion and Formation of Coupled Electron Hole and Ion-Acoustic Soliton in a Plasma, *Physical Review Letters* **80**, 1224 (1998).
- [12] I. H. Hutchinson, Electron holes in phase space: What they are and why they matter, *Physics of Plasmas* **24**, 055601 (2017).

- [13] C. Zhou and I. H. Hutchinson, Plasma electron hole ion-acoustic instability, *J. Plasma Phys.* **83**, 905830501 (2017), arXiv:arXiv:1701.03140v1 .
- [14] C. Zhou and I. H. Hutchinson, Dynamics of a slow electron hole coupled to an ion-acoustic soliton, *Physics of Plasmas* **25**, 082303 (2018).
- [15] N. Jain, T. Umeda, and P. H. Yoon, Modeling nonlinear development of Buneman instability with linear dispersion theory, *Plasma Physics and Controlled Fusion* **53**, 025010 (2011).
- [16] R. S. Rajawat and S. Sengupta, Particle-in-cell simulation of Buneman instability beyond quasilinear saturation, *Physics of Plasmas* **24**, 122103 (2017).
- [17] K. Hara and C. Treece, Ion kinetics and nonlinear saturation of current-driven instabilities relevant to hollow cathode plasmas, *Plasma Sources Science and Technology* **28**, 055013 (2019).
- [18] A. Tavassoli, M. Shoucri, A. Smolyakov, M. Papahn Zadeh, and R. J. Spiteri, Backward waves in the nonlinear regime of the Buneman instability, *Physics of Plasmas* **28**, 022307 (2021).
- [19] D. Biskamp and R. Chodura, Computer Simulation of Anomalous dc Resistivity, *Physical Review Letters* **27**, 1553 (1971).
- [20] C. Dum and R. Chodura, Anomalous transition from buneman to ion sound instability, in *Wave Instabilities in Space Plasmas*, edited by P. J. Palmadesso and K. Papadopoulos (D. Reidel Publishing Company, 1978) p. 135.
- [21] J. Büchner and N. Elkina, Anomalous resistivity of current-driven isothermal plasmas due to phase space structuring, *Physics of Plasmas* **13**, 082304 (2006).
- [22] Y. Omura, W. J. Heikkila, T. Umeda, K. Ninomiya, and H. Matsumoto, Particle simulation of plasma response to an applied electric field parallel to magnetic field lines, *Journal of Geophysical Research: Space Physics* **108**, 10.1029/2002JA009573 (2003).
- [23] H. Che, J. F. Drake, M. Swisdak, and P. H. Yoon, Electron holes and heating in the reconnection dissipation region, *Geophysical Research Letters* **37**, 10.1029/2010GL043608 (2010).
- [24] A. R. Niknam, D. Komaizi, and M. Hashemzadeh, Simulation of low frequency Buneman instability of a current-driven plasma by particle in cell method, *Physics of Plasmas* **18**, 022301 (2011).
- [25] H. Che, J. F. Drake, M. Swisdak, and M. L. Goldstein, The adiabatic phase mixing and heating of electrons in Buneman turbulence, *Physics of Plasmas* **20**, 061205 (2013).
- [26] J. Chen, A. V. Khrabrov, I. D. Kaganovich, and H.-P. Li, Intermittency, bursty turbulence, and ion and electron phase-space holes formation in collisionless current-carrying plasmas, *Physics of Plasmas* **31**, 042112 (2024).

- [27] Z. Liu, R. White, M. Francisquez, L. M. Milanese, and N. F. Loureiro, A two-dimensional numerical study of ion-acoustic turbulence, *Journal of Plasma Physics* **90**, 965900101 (2024).
- [28] I. H. Hutchinson, Nonlinear collisionless plasma wakes of small particles, *Phys. Plasmas* **18**, 032111 (2011).
- [29] I. H. Hutchinson, Transverse instability magnetic field thresholds of electron phase-space holes, *Physical Review E* **99**, 053209 (2019).
- [30] O. Buneman, Dissipation of Currents in Ionized Media, *Physical Review* **115**, 503 (1959).
- [31] H. Schamel, Hole equilibria in Vlasov–Poisson systems: A challenge to wave theories of ideal plasmas, *Physics of Plasmas* **7**, 4831 (2000).
- [32] H. Schamel, Cnoidal electron hole propagation: Trapping, the forgotten nonlinearity in plasma and fluid dynamics, *Physics of Plasmas* **19**, 020501 (2012).
- [33] A. A. Vedenov, E. P. Velikhov, and R. Z. Sagdeev, Nonlinear oscillations of rarified plasma, *Nuclear Fusion* **1**, 82 (1961).
- [34] R. Z. Sagdeev, Cooperative Phenomena and Shock Waves in Collisionless Plasmas, *Reviews of Plasma Physics* **4**, 23 (1966), aDS Bibcode: 1966RvPP...4...23S.
- [35] It has been noted recently, e.g. in [36] and references therein, that pseudo-potential treatments like this (though with $v_{de} = 0$) of nonlinear ion acoustic waves have often ignored the fact that $\langle n \rangle$ is not exactly equal to the reference density that has been used to define the length scale λ_{De} . However, since the treatment here in terms of the normalized \hat{V} shows that the absolute density does not enter into the determination of $\phi_{max} - \phi_{min}$, it is clear that any discrepancy amounts only to a straightforward adjustment of the length (and time) scaling.
- [36] A. E. Dubinov, On One Widely-Spread Inaccuracy and Its Elimination in the Theories of Nonlinear Electrostatic Waves in Plasma Based on the Sagdeev’s Pseudopotential Approach, *Plasma Physics Reports* **49**, 362 (2023).